Unexpected role of singlet oxygen generated in urea-modulated LaFeO$_3$ perovskite heterogeneous Fenton system in denitrification: Mechanism and theoretical calculations

Zhen Qian [a,b], Mengchao Luo [a], Xiaohe Feng [a], Xiaojie Yang [a], Yongxue Guo [a], Lijuan Yang [a,b], Bo Yuan [a,b], Yi Zhao [a,b], Runlong Hao [a,b,*]

[a] Hebei Key Lab of Power Plant Flue Gas Multi-Pollutants Control, Department of Environmental Science and Engineering, North China Electric Power University, Baoding 071003, PR China
[b] MOE Key Laboratory of Resources and Environmental Systems Optimization, College of Environmental Science and Engineering, North China Electric Power University, Beijing 102206, PR China

ARTICLE INFO

ABSTRACT

This study appears an unprecedented phenomenon that $^1O_2$, generated in urea-modulated LaFeO$_3$ (U-LaFeO$_3$) perovskite heterogeneous Fenton system, is superior to OH• and $O_2\bullet^-$ in NO removal. The 2.5 U-LaFeO$_3$/H$_2$O$_2$ system can remove 82.9% of NO, with a low H$_2$O$_2$/NO molar ratio (4.7) and high GHSV (30,800 h^{-1}), along with good environmental adaptability and reusability. Urea modulation induced the formations of abundant La defects, O vacancies and Fe(IV), also improved the pore structure and surface area. The contribution order of different free radicals to NO removal is $^1O_2 > xO_2\bullet^- > \bullet OH$. Characterization combined with theoretical calculation clarify that (i) H$_2$O$_2$ is inclined to derive HO$_2$• on Fe sites; (ii) $^1O_2$ is mainly generated from $O_2\bullet^-$ reaction with Fe(IV)/Fe(III); (iii) •OH is mainly produced by splitting of H$_2$O$_2$ on Fe site and decomposition of HO$_2$• on OV site. The main denitrification paths are NO+$^1O_2 \rightarrow$ NO$_2$, NO$_2$ + •OH$\rightarrow$NO$_3$ and NO+ •OH$\rightarrow$NO$_2^-$.

1. Introduction

As a primary atmospheric pollutant, nitrogen oxides (NOx, composed of ~95% NO) are the main precursors for ozone, photochemical smog, haze and other environmental issues, posing enormous threats to human health [1,2]. To reduce NOx emissions from stationary source, the mature selective catalytic reduction (SCR) and selective non-catalytic reduction (SNCR) technologies have been widely applied, but they still cannot be adaptive for all working conditions due to narrow applicable temperature ranges [2–5]. In some cases, the SCR or SNCR alone is very difficult to meet ultra-low emission standard of NOx ($\leq$50 mg/m^3). Hence, developing low temperature denitrification method that can couple with the SCR or SNCR system to realize deep removal of NOx is urgently needed. In this respect, advanced oxidation process (AOP) is a good supplement [6,7].

Past cognition always believes that in Fenton or Fenton-like AOP system, NO oxidation induced by hydroxyl radical (HO•) is the most efficient reaction path [8], and hydrogen peroxide (H$_2$O$_2$) is often used as the precursor due to its advantages of low cost and environmental friendly [9]. To boost the HO• yield and increase the H$_2$O$_2$ utilization, various Fe-based materials (e.g., Fe^0, Fe$_2$O$_3$, Fe$_3$O$_4$, Co-Fe, Cu-Fe, Mn-Fe and FeOOH, etc) and different catalytic modes (e.g., heat, light, electricity and ultrasound, ets) have been developed and used [10–13]. However, their catalytic activity towards H$_2$O$_2$ is still not so good due to the inefficient circulation of Fe(II)/Fe(III) and the great loss of H$_2$O$_2$ during the radicals back-forth conversion [6]. On the other hand, in terms of the reactivity of various reactive oxygen species (ROS), more and more researchers have been aware of that the non-radical singlet oxygen ($^1O_2$) with longer lifetime (about 4 us), higher selectivity and stronger reactivity [14,15], appears superior ability than •OH (shorter lifetime, 10^{-3} us, and nonselective) in the degradation of electron-rich water organic pollutants and certain volatile organic compounds (VOCs), thus $^1O_2$ has attracted increased attention in recent years. According to the quantum chemistry calculation, we also demonstrated that $^1O_2$ could act as a bridge to boost the NO conversion process via lowering the energy barrier from NO to NO$_3$, but the formation of $^1O_2$

---

from the direct activation of H_2O_2 was still a challenge. To date, $^1O_2$ is mainly generated by the activation of peroxymonosulfate (PMS) using heterogeneous catalysts, such as CoN_{2+2}, Cu-SA/MXene, Fe/O-doped g-C_3N_4, et al. [16–18]. The asymmetric PMS (HO-O-SO$_3^-$) has three types of O atoms, which can provide different O atom coordination for catalysts, resulting in different trends of O-O and O-H breakage during PMS activation, thus can selectively split PMS to generate $^1O_2$ by modulating the coordination environment of the catalyst with O atoms [18,19]. In contrast, the symmetrical structure of H_2O_2 (HO-OH) with two identical O atoms cannot form differential O coordination with the catalytic site, so it is difficult to activate H_2O_2 generating multiple ROS, especially $^1O_2$ [19].

The latest researches clarified that high-valent oxides such as Co^{4+} and Mo^{6+} were capable of activating superoxide radicals ($O_2\bullet^-$) to generate $^1O_2$ [20,21]. It is lucky that ABO$_3$-type perovskite iron oxides (LaFeO$_3$) contains high-valent iron state Fe(IV) and also can activate H_2O_2 into $O_2\bullet^-$ [22], thus LaFeO$_3$ with more Fe(IV) sites may be a good candidate for catalyzing H_2O_2 to directly generate $^1O_2$. However, the number of high-valent B-sites exposed by normal perovskite is limited, a modulation strategy is needed to further increase the number of high-valent B-sites exposed. Surface defects engineering can improve the electronic structure and surface chemical property of the normal perovskite materials, which can empower the perovskite catalyst with excellent ability of electron transfer and reactants adsorption [23,24]. For example, (i) A-site defect produced via doping or substitution methods, e.g. introducing Sr, Ca and Cu atoms into A-site to modulate its structure, can greatly improve its catalytic activity toward H_2O_2 and PMS to yield more ROS [25,26]; (ii) non-doping methods like non-stoichiometric strategy [27,28], urea modulation configuration and surface acid etching can boost the oxygen vacancy (OV) quantity [29,30], improve the pore structure and increase the surface area, which can strengthen the mass transfer and reactants adsorption as well as possibly increasing the ROS yield. Hence, integrated utilization/modulation of these modification methods to develop an advanced Fe-based perovskite heterogeneous Fenton catalyst may yield a large number of $^1O_2$ from H_2O_2 activation and also achieve a better NO removal performance.

Herein, the present study prepared a novel LaFeO$_3$ heterogeneous Fenton catalyst via modulating its surface defects using non-stoichiometric and urea treatment methods, from which the abundant A-site defects, OVs and Fe(IV) active sites on the surface were formed simultaneously. In particular, urea-modulated LaFeO$_3$ could effectively activate H_2O_2 to generate $^1O_2$, which was found to be superior to $\bullet OH$ and $O_2\bullet^-$ in NO removal, and this LaFeO$_3$/H_2O_2 system achieved the cost-effective removal of NO, with high gas hourly space velocity (GHSV) and low H_2O_2/NO molar ratio. Based on the characterization and theoretical calculation results, the mechanisms of urea-modulated LaFeO$_3$ activating H_2O_2 to generate various ROS and the NO removal induced by different ROS were proposed.

2. Experimental Section

2.1. Synthesis of catalysts

All reagents used in this study are listed in Text S1. LaFeO$_3$, La$_x$FeO$_3$ (x = 0.6, 0.7, 0.8, 0.9) and xU-LaFeO$_3$ (x = 1, 2.5, 3.5, 5) were synthesized via one-pot sol-gel method [24], and the fabrication scheme of these materials was shown in Fig. 1. (i) *Synthesis of LaFeO$_3$*: 2.60 g La (NO$_3$)$_3$·6 H$_2$O and 2.43 g Fe(NO$_3$)$_3$·9 H$_2$O were dissolved in 40 mL of deionized water at room temperature under stiffing for 3 h. Subsequently, 2.78 g citric acid was added and stirred vigorously at 80 °C until the sol was formed, then this sol was dried overnight at 110 °C to obtain the spongy-like solid, which was ground and calcined in a muffle furnace at 700 °C for 5 h. (ii) *Synthesis of La$_x$FeO$_3$*: the procedure was identical to the LaFeO$_3$ synthesis, except that the amount of La(NO$_3$)$_3$·6 H$_2$O added was different. The obtained products were named as La$_{0.6}$FeO$_3$, La$_{0.7}$FeO$_3$, La$_{0.8}$FeO$_3$ and La$_{0.9}$FeO$_3$, respectively, with respect to the molar ratio of La/Fe of 0.6, 0.7, 0.8 and 0.9. (iii) *Synthesis of xU-LaFeO$_3$*: the procedure was the same as the LaFeO$_3$ synthesis, except that a certain amount of urea was added to the synthesis process. Specifically, when the molar ratio of urea and La+Fe was 1, 2.5, 3.5 and 5, the obtained products were named as U-LaFeO$_3$, 2.5 U-LaFeO$_3$, 3.5 U-LaFeO$_3$ and 5 U-LaFeO$_3$, respectively. The synthesis of 2.5 U-LaMnO$_3$ was the same as that of 2.5 U-LaFeO$_3$, except that Fe(NO$_3$)$_3$·9 H$_2$O was replaced to Mn(NO$_3$)$_2$ solution in the synthesis process.

2.2. Characterization methods

The actual compositions of sample was determine by Inductively Coupled Plasma Optical Emission Spectrometer (ICP-OES) technique (PE-7000DV, USA); the phase and crystal structure of samples were obtained by X-ray diffractometer (XRD, Bruker D8 advance); the surface chemical composition was analyzed by Fourier Transform Infrared
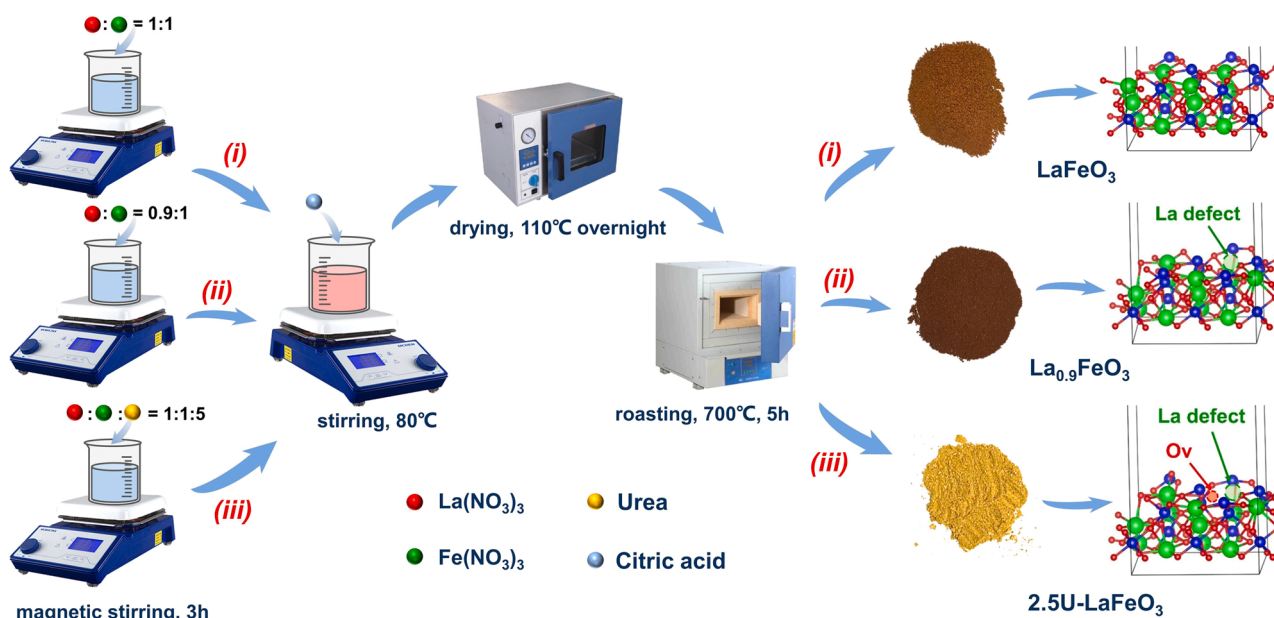

Fig. 1. Schematic illustration of the synthesis process of LaFeO$_3$, La$_{0.9}$FeO$_3$ and 2.5 U-LaFeO$_3$ catalysts.

Spectroscopy(FT-IR, Bio-Rad FTS-6000). The morphologies of materials were observed by scanning electron microscope (SEM, JSM-7500 F), high-resolution transmission electron microscopy (HRTEM, JEM-2100) and EDX elemental mapping. The nitrogen adsorption-desorption isotherms were applied to analyze the specific surface area, pore size and pore capacity of the catalysts; X-ray photoelectron spectroscopy (XPS, ESCALAB 250Xi) and energy spectroscopy (EDX) were used to analyze the active components on the catalyst surface. The reducibility and oxidizability of the samples were characterized by H_2 temperature programmed reduction (H_2-TPR) and O_2 temperature programmed desorption (O_2-TPD), respectively; the surface charge of samples were recorder by the Zeta potential analyzer. The yield of oxygen vacancy (Ov) and the radical species in the reaction system were identified by electron spin resonance spectrometer(EPR, Bruker EMX-E spectrometer). The ^{57}Fe Mössbauer spectra of compounds 1 and 2 were recorded on an SEE Co W304 Mössbauer spectrometer, using a ^{57}Co/Rh source in transmission geometry. The data were fitted by using the MossWinn 4.0 software.

2.3. Experimental procedure

The experimental flow is shown in Fig. S1, which consists of three parts: the simulated flue gas generation unit, the catalytic oxidation-absorption unit and the exhaust gas detection unit, all pipelines are made by Teflon. The simulated flue gas consists of N_2, NO, SO_2, CO_2 and O_2 with the total flow rate of 1 L/min, controlled by reducing valves and mass flow controllers. To generate the vaporized oxidant, the H_2O_2 solution was continuously pumped into a self-made evaporation reactor by a peristaltic pump at a rate of 256 μL/min and vaporized by a thermally controlled electric heater. The vaporized oxidant was then carried by the simulated flue gas into a quartz tube (the diameter of 1 cm, the length of 400 cm) heated by a tube furnace, where the NO catalytic oxidation reaction occurred, and then the oxidation products were absorbed by 150 mL of 0.24 M Na_2SO_3 solution or H_2O. In addition, the catalyst dosage for each denitrification experiment was 0.1 g, while the gas hourly space velocity (GHSV) was 77,000 h^{-1}. The flue gas concentration was recorded by a multifunctional flue gas analyzer, and the NO removal efficiency was calculated via Eq. 1, and the molar ratio of H_2O_2/NO was obtained via Eq. 2:

$$\eta = \frac{C_{in} - C_{out}}{C_{in}} \times 100\% \tag{1}$$

$$\delta = \frac{n_{H_2O_2}}{n_{NO}} = \frac{\frac{\omega \times \rho_{H_2O_2} \times V_{H_2O_2}}{34}}{\frac{C_{NO} \times Q}{30}} \tag{2}$$

Where η is the NO removal efficiency; C_{in} and C_{out} are the inlet and outlet concentrations of NO, mg/m^3; δ is the molar ratio of H_2O_2/NO; ω is the mass fraction of H_2O_2, wt%; ρ_{H2O2} is the density of H_2O_2; V_{H2O2} is the volume of H_2O_2, uL/min; C_{NO} is the NO concentration, mg/m^3; Q is the flue gas flow, m^3/min.

2.4. Density functional theory (DFT) calculation

DFT was performed using the Vienna ab initio Simulation Package (VASP). The interactions of core and nucleus with valence electrons are treated by the projective augmented wave (PAW) method, and the exchanges and correlations are described using the Perdew- Burke- Ernzerhof (PBE) functional. The (110) facet of LaFeO$_3$ was built with 2×1 supercell, and a vacuum layer of 15 Å was added to separated neighboring slabs to avoid possible interaction. Sampling of the Brillouin zone using a $2 \times 2 \times 1$ mesh of Monkhorst-Pack k-points for structural relaxation. The plane-wave cutoff energy was set at 400 eV. In the fully relaxed structure, the forces acting on all atoms were < 0.02 eV/ Å, and the electronic loops were self-consistent to an accuracy of 10^{-5} eV. The spin polarization of transition metal atoms was also considered. To

obtain the transition state structure, the climbing-image nudged elastic band (Cl-NEB) method was adopted, and the vibration frequency analysis was performed using a finite displacement of ± 0.02 Å to verify the minima and transition state structure. The configurations of La$_{0.9}$FeO$_3$ and 2.5 U-LaFeO$_3$ were constructed based on the orthorhombic LaFeO$_3$ system. One La atom was removed in the LaFeO$_3$ supercell to match the experimental composition La$_{0.9}$FeO$_3$, and one La and O atom were removal simultaneously to match 2.5 U-LaFeO$_3$. The adsorption strength of gas molecules on the catalyst surface was calculated using Eq. 3:

$$E_{ads} = E_{adsorb} - E_{sur} - E_{gas} \tag{3}$$

where E_{adsorb}, E_{sur} and E_{gas} are the total energies of adsorption systems, catalyst surface and gases, respectively.

To describe the possible reaction pathways for HO•, O_2•⁻, HO$_2$• and $^1O_2$ induced NO removal, DFT (MP2) calculations were performed using the Gaussian program package (G09W), and the reaction energy barriers for each step were calculated to predict the difficulty of each reaction from its energy perspective. The reliability was verified by frequency calculations of vibrational modes, and the performance of NO oxidation by HO•, O_2•⁻, HO$_2$• and $^1O_2$ was predicted thermodynamically. Gaussian calculations were performed at the 6–311 G (d, p) basis group level.

3. Results and discussion

3.1. Catalysts characterizations

The elemental proportions of LaFeO$_3$, La$_{0.9}$FeO$_3$ and 2.5 U-LaFeO$_3$ were analyzed by ICP-OES. In Fig. 2(a) and Table S1, the molar ratio of La to Fe is 0.96 (LaFeO$_3$) > 0.91 (La$_{0.9}$FeO$_3$) > 0.87 (2.5 U-LaFeO$_3$), confirming that urea modulation and non-stoichiometric synthesis could lead to the La-site defects. Owing to the similar size, NH^{4+} (1.44 Å) generated via urea pyrolysis can replace part of La^{3+} (1.36 Å) in LaFeO$_3$, and has a weak interaction with the surface FeO$_6$ octahedra, leading to the formation of N-H-O-Fe staggered conformation [31,32]. Besides, during urea pyrolysis process, N-H can also migrate out from the crystalline phase, resulting in the formations of La and O defects. In Fig. S2, the N 1 s XPS spectra of LaFeO$_3$, La$_{0.9}$FeO$_3$ and 2.5 U-LaFeO$_3$ and the EDX spectrum of 2.5 U-LaFeO$_3$ reveal the absence of N species on 2.5 U-LaFeO$_3$ surface, further confirming that urea can migrate out from the perovskite crystal phase at high temperature. The crystalline phases of the three catalysts were characterized by XRD. In Fig. 2(b), all of the three catalysts have the same and obvious characteristic peaks at 22.63, 32.22, 39.73, 46.21, 52.04, 57.45, 67.41, 76.70 and 85.63°, corresponding to the diffraction planes of (100), (110), (111), (200), (210), (211), (220), (310) and (222), respectively, indicating the LaFeO$_3$ orthorhombic crystal phase (PDF# 75–0541). Their phase structures were also determined by XRD Rietveld refinement (Fig. S3), demonstrating their orthorhombic symmetry with a *Pnma* space group. Their FT-IR spectra all appear strong adsorption peaks at 553 cm^{-1} (Fig. S4), attributing to the Fe-O stretching vibration of the FeO$_6$ group [33]. Thus, the urea modulation and non-stoichiometric synthesis did not change the bulk phase structure of the catalysts.

The morphological and microstructural features of LaFeO$_3$, La$_{0.9}$FeO$_3$ and 2.5 U-LaFeO$_3$ were imaged by SEM and HRTEM. In Fig. 2 (c), the three samples all appear in the form of smooth wormlike rods, while 2.5 U-LaFeO$_3$ is more porous and well dispersed. In Fig. 2(d), LaFeO$_3$ has normal interface, while La$_{0.9}$FeO$_3$ and 2.5 U-LaFeO$_3$ appear defects, and the lattice fringe size of the primary (110) facet is decreased from 0.284 nm (LaFeO$_3$) to 0.283 nm (La$_{0.9}$FeO$_3$) and 0.281 nm (2.5 U-LaFeO$_3$), suggesting that modulation process smaller the lattice fringe spacing and caused the lattice distortion. The increase in the surface and edge defects due to urea modulation and non-stoichiometric synthesis will be favorable to increase the active sites for reactants adsorption [34,
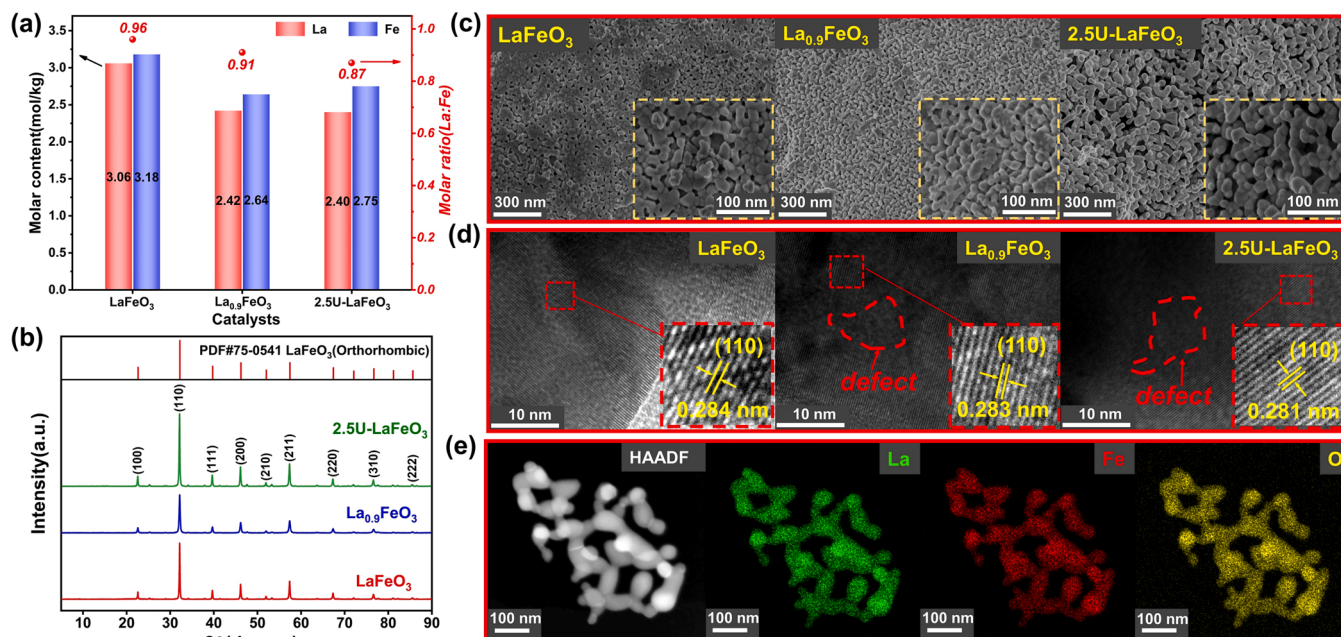
Fig. 2. (a) Molar content and the ratio of La to Fe in $LaFeO_3$, $La_{0.9}FeO_3$ and 2.5 U-$LaFeO_3$; (b) XRD patterns of $LaFeO_3$, $La_{0.9}FeO_3$ and 2.5 U-$LaFeO_3$; (c) SEM and (d) HRTEM images of $LaFeO_3$, $La_{0.9}FeO_3$ and 2.5 U-$LaFeO_3$; (e) EDX element mapping images of 2.5 U-$LaFeO_3$.

35]. In Fig. 2(e), the EDX mappings confirms the uniform distribution of La, Fe, and O on the surface of 2.5 U-$LaFeO_3$. In Fig. 3(a), the nitrogen adsorption-desorption isotherms of $LaFeO_3$, $La_{0.9}FeO_3$, and 2.5 U-$LaFeO_3$ illuminate that all curves belong to the type IV hysteresis line (H3 type) according to the IUPAC [36], indicating that the three catalysts are mesoporous materials. The surface area in descending order is $29.278 \, m^2/g$ (2.5 U-$LaFeO_3$) > $8.137 \, m^2/g$ ($La_{0.9}FeO_3$)

> $7.634 \, m^2/g$ ($LaFeO_3$), as consistent with the variation in the pore volume. However, the pore diameter has an opposite order: 13.158 nm (2.5 U-$LaFeO_3$) < 17.449 nm ($La_{0.9}FeO_3$) < 23.500 nm ($LaFeO_3$). Due to its largest specific surface area and best pore structure, 2.5 U-$LaFeO_3$ could expose the most active sites to boost the catalytic reaction by enabling better access to both reactants and peroxide [27].

The surface chemical compositions and elemental valence state of
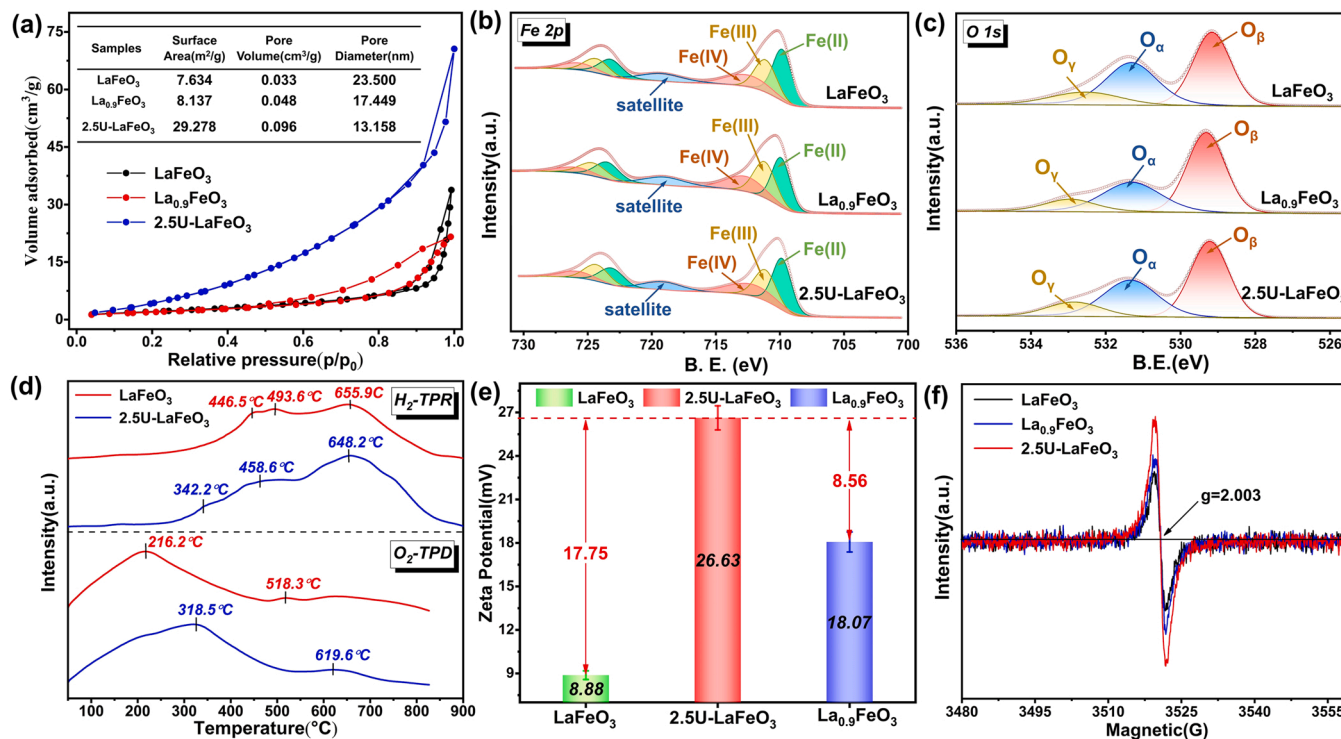
Fig. 3. (a) The nitrogen adsorption-desorption isotherms of $LaFeO_3$, $La_{0.9}FeO_3$, and 2.5 U-$LaFeO_3$, the inset table is the specific surface area and pore characteristic of these three samples; (b) Fe 2p and (c) O 1 s XPS spectra of $LaFeO_3$, $La_{0.9}FeO_3$, and 2.5 U-$LaFeO_3$: (d) O_2-TPD and H_2-TPR cures of $LaFeO_3$ and 2.5 U-$LaFeO_3$; (e) Zeta potential and (f) EPR spectra of $LaFeO_3$, $La_{0.9}FeO_3$, and 2.5 U-$LaFeO_3$.

LaFeO$_3$, La$_{0.9}$FeO$_3$ and 2.5 U-LaFeO$_3$ were further determined by XPS. In Fig. S5, the La 3d XPS spectra of the three catalysts all show four main peaks at 854.9, 851.8, 838.0 and 834.2 eV, corresponding to the La(III) 3d$_{3/2}$, La(II) 3d$_{3/2}$, La(III) 3d$_{5/2}$ and La(II) 3d$_{5/2}$ [31,37]. In Table S2, the La(II) contents of LaFeO$_3$, La$_{0.9}$FeO$_3$ and 2.5 U-LaFeO$_3$ are 47.80%, 51.99% and 49.10%, respectively, which are 52.20%, 48.01% and 50.90% for La(III), indicating that non-stoichiometric synthesis and urea modulation would result in the conversion of partial La(III) to La(II). The Fe 2p XPS spectra in Fig. 3(b) can be resolved into six main peaks, in which Fe 2p$_{3/2}$ at 709.8 eV and Fe 2p$_{1/2}$ at 723.2 eV are assigned to Fe (II), Fe 2p$_{3/2}$ at 711.1 eV and Fe 2p$_{1/2}$ at 724.3 eV are attributed to Fe (III), and Fe 2p$_{3/2}$ at 712.6 eV and Fe 2p$_{1/2}$ at 725.8 eV are corresponding to Fe(IV). Besides, the peak located at 719.2 eV is a satellite peak [38,39]. In Table S2, the concentrations of Fe(II)/Fe(III)/Fe(IV) of LaFeO$_3$ are 45.11%, 32.02% and 22.87%, respectively, which are varied to 39.29%, 35.48% and 25.23% for La$_{0.9}$FeO$_3$, and to 41.01%, 33.46% and 25.53% for 2.5 U-LaFeO$_3$, suggesting that non-stoichiometric synthesis and urea modulation leaded to the conversion of Fe(II) to Fe (III)/Fe(IV) because of the formations of La and O defects. Such increase in the valence of the B-site cation will enhance the catalyst's oxidizability via facilitating the electron transfer between the reactants and the catalyst [39]. The O 1 s XPS spectra in Fig. 3(c) can be divided into three peaks at 529.2, 531.3 and 532.8 eV, corresponding to the lattice oxygen (O$_\beta$), the surface chemisorbed oxygen (O$_\alpha$), and the physically adsorbed oxygen such as water and other weakly bounded oxygen species (O$_\gamma$), respectively [31,38]. In Table S2, the O$_\alpha$ content in descending order is 38.64% (LaFeO$_3$) > 34.16% (2.5 U-LaFeO$_3$) > 31.22% (La$_{0.9}$FeO$_3$), implying that both of non-stoichiometric synthesis and urea modulation would decrease the O$_\alpha$ content.

O$_2$-TPD is employed to investigate the distribution of oxygen species on the catalysts. In Fig. 3(d), two O$_2$ desorption peaks are clearly observed on LaFeO$_3$ and 2.5 U-LaFeO$_3$. The first peak at 216.2 °C for LaFeO$_3$ and at 318.5 °C for 2.5 U-LaFeO$_3$ is attributed to the desorption of surface active oxygen species [40–42], and such high temperature shift after urea modulation is due to the increase in oxygen vacancies (OVs) which stronger the bond with O$_2$ [27]. The second weak peak at 518.3 °C for LaFeO$_3$ and at 619.6 °C for 2.5 U-LaFeO$_3$ is assigned to the desorption of lattice oxygen in bulk phase [42], and the increase in desorption temperature after urea modulation is because the Fe-O bond becomes shorter owing to the La cation stripping [30]. The oxidizing capacity of LaFeO$_3$ and 2.5 U-LaFeO$_3$ were also studied by H$_2$-TPR in Fig. 3(d). Generally, La^{3+} is less susceptible to reduction below 1000 °C, so the reduction peaks observed in the TPR curves are attributed to the reduction of Fe species [40,43]. Three H$_2$ desorption peaks can be observed, in which the former two peaks below 550 °C are attributed to the reductions of Fe(IV) to Fe(III) and the surface Fe(III) to Fe(II), respectively, while the latter one peak above 550 °C belongs to the reductions of bulk Fe(III) to Fe(II) and Fe(II) to Fe(0) [43,44]. It can also be found that the urea treatment remarkably decreases the desorption temperatures from 446.5 to 342.2 °C and from 493.6 to 458.6 °C, respectively, indicating that the oxidizing capacity of Fe(IV) and the surface Fe(III) becomes stronger after urea treatment.

The surface charge of the three catalysts was determined by using Zeta potential method. In Fig. 3(e), the Zeta potential of 2.5 U-LaFeO$_3$ is 26.63 mV, which is far higher than those of La$_{0.9}$FeO$_3$ (18.07 mV) and pure LaFeO$_3$ (8.88 mV), indicating that the urea-modulated LaFeO$_3$ possessed the strongest adsorption capacity towards H$_2$O$_2$. Generally, the more positively charged surface of the oxide, the more anionic surface defects may appear, namely OV [27]. So we further used EPR analysis to investigate the OV quantity on the surface of LaFeO$_3$, La$_{0.9}$FeO$_3$ and 2.5 U-LaFeO$_3$. In Fig. 3(f), the OV's peak intensity of 2.5 U-LaFeO$_3$ (19,852.46) is about 1.5 and 1.8 times as much as those of La$_{0.9}$FeO$_3$ (13,749.57) and LaFeO$_3$ (11,119.49), implying that urea modulation indeed facilitated the OVs' construction, and this result also well supported the O$_2$-TPD and Zeta potential analyses.

3.2. Heterogeneous Fenton denitrification performance

The heterogeneous Fenton denitrification performance of La$_2$O$_3$, Fe$_3$O$_4$, Fe$_2$O$_3$, LaFeO$_3$, La$_{0.9}$FeO$_3$, 2.5 U-LaFeO$_3$ and 2.5 U-LaMnO$_3$ were compared in Fig. 4(a). The NO removal efficiency is merely 37.09% when only using 3 wt% H$_2$O$_2$; after adding catalysts, the NO removal efficiency sharply increases to 50.49%, 60.01%, 61.16%, 65.64%, 69.83%, 80.53% and 54.56% with respect to the catalysts of La$_2$O$_3$, Fe$_3$O$_4$, Fe$_2$O$_3$, LaFeO$_3$, La$_{0.9}$FeO$_3$, 2.5 U-LaFeO$_3$ and 2.5 U-LaMnO$_3$, apparently 2.5 U-LaFeO$_3$ is the best. In Fig. 3(a) and S6, the surface area in descending order is 1.870 m^2/g (La$_2$O$_3$) < 6.914 m^2/g (Fe$_2$O$_3$) < 7.634 m^2/g (LaFeO$_3$) < 8.057 m^2/g (Fe$_3$O$_4$) < 8.137 m^2/g (La$_{0.9}$FeO$_3$) < 29.278 m^2/g (2.5 U-LaFeO$_3$) < 46.823 m^2/g (2.5 U-LaMnO$_3$), which is not consistent with the denitrification performance, indicating that the increase in specific surface area is not the main reason for the improvement of catalytic activity. Fig. 4(b) illustrates the effect of the urea ratio on NO removal. The NO removal efficiency increases from 74.48% to 80.53% as the urea ratio increases from 1 to 2.5, and then decreases to 71.08% as the ratio further increases to 5. This phenomenon indicated that the excess urea was unfavorable for NO removal due to the pore blockage and the decrease in specific surface area, as demonstrated in Fig. S7. On the other hand, if without H$_2$O$_2$, the NO removal efficiency by using 2.5 U-LaFeO$_3$ was only 7.12%, indicating that 2.5 U-LaFeO$_3$ alone was also inefficiently in removing NO. The NO removal performance by using non-stoichiometric La$_x$FeO$_3$ (x = 0.6, 0.7, 0.8, 0.9, 1.0) catalysts is also shown in Fig. S8. The results showed that the La$_{0.9}$FeO$_3$ was the best (69.83%) but still far from that of 2.5 U-LaFeO$_3$ (80.53%), thereby the urea modulation method was better than the non-stoichiometric synthesis method in terms of improving the Fenton activity.

The effects of GHSV and the H$_2$O$_2$ concentration on NO removal were also studied in Figs. S9 and 4(c). When the GHSV decreases from 92,400 to 30,800 h^{-1}, the NO removal efficiency increases sharply from 45.61% to 82.89%; raising the H$_2$O$_2$ concentration from 1%wt to 5%wt (the H$_2$O$_2$/NO molar ratio increases from 4.7 to 24.0) can increase the NO removal efficiency from 82.89% to 94.74%. In Table S3, we can find that 2.5 U-LaFeO$_3$/H$_2$O$_2$ developed in this study is superior to the previous similar studies in NO removal, especially the lowest H$_2$O$_2$/NO molar ratio and the relatively high GHSV value. In the following parts, the GHSV and the H$_2$O$_2$ concentration were selected as 77,000 h^{-1} and 5% wt, respectively. Fig. 4(d) illuminates the effect of the reaction temperature: a 'volcano map' curve between the NO removal efficiency and the temperature is observed, the best temperature is 120 °C for both H$_2$O$_2$ vaporization denitrification (37.07%) and 2.5 U-LaFeO$_3$ induced heterogeneous Fenton denitrification (89.12%). Fig. S10 clarifies the effect of pH on NO removal: acidic conditions promote NO removal, and neutral has basically no effect, but alkaline conditions slightly inhibit NO removal. The 2.5 U-LaFeO$_3$ heterogeneous Fenton denitrification system is adaptive to a wide pH range and is superior to the conventional Fenton system [45]. In Fig. 4(e), NO, O$_2$ and CO$_2$ exhibit the slight inhibitory effects but SO$_2$ plays a favorable role in NO removal, indicating that NO, O$_2$ and CO$_2$ would compete with H$_2$O$_2$ for the limited active sites, however SO$_2$ could enhance the NO removal via the redox reaction between SO$_2$ and NO$_2$ under moisture atmosphere [46]. Besides, it can be observed from Fig. S11 that the promoting effect of SO$_2$ can cover up the inhibiting effect of O$_2$, and the NO removal efficiency is enhanced when O$_2$ and SO$_2$ are added simultaneously. After withdrawing O$_2$ and SO$_2$, the NO removal efficiency gradually recover to the initial level, indicating the stability of 2.5 U-LaFeO$_3$ denitrification performance. In Fig. 4(f), the reusability of 2.5 U-LaFeO$_3$ was evaluated, and the NO removal efficiency decreases only by 7% after fifth cycle. Moreover, the XRD and SEM patterns of the spent 2.5 U-LaFeO$_3$ shown in Figs. S12-S13 appear no significant variations in the crystalline phase and morphology, implying that 2.5 U-LaFeO$_3$ had excellent stability and reusability.
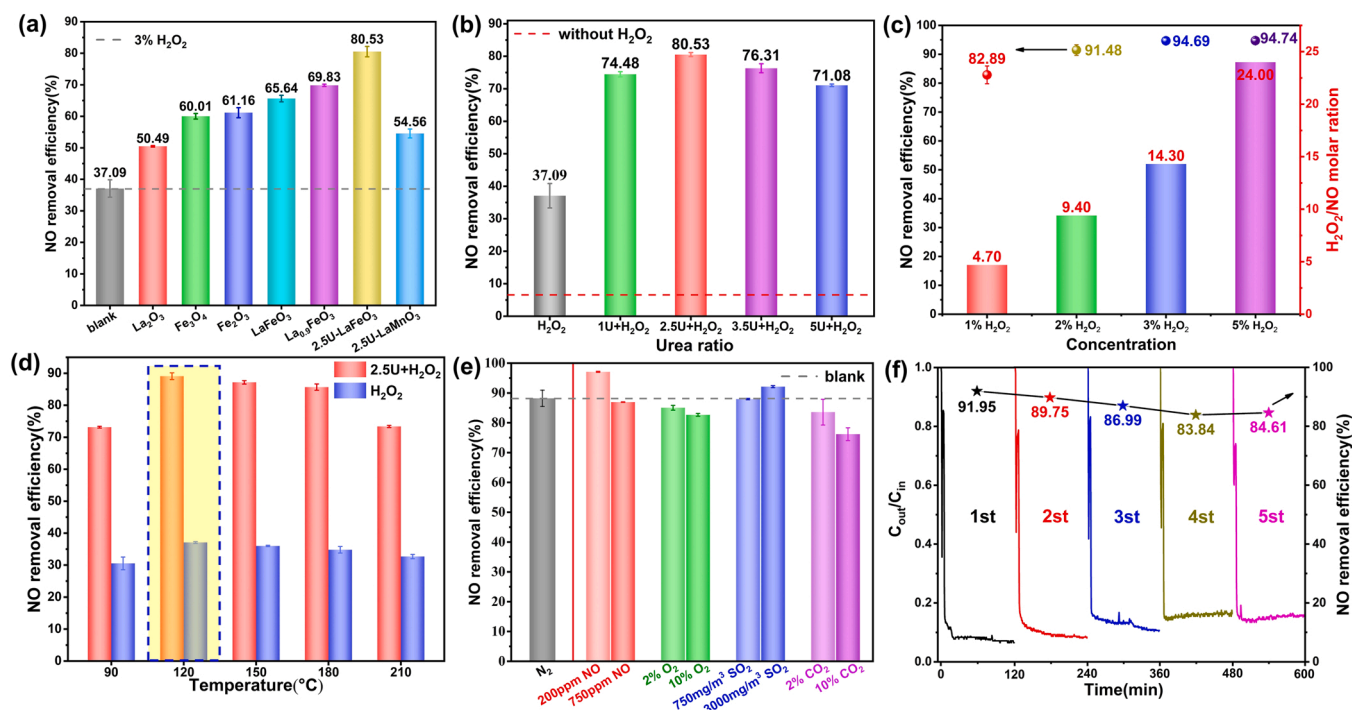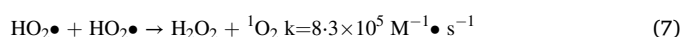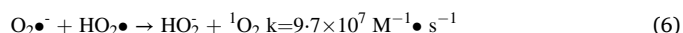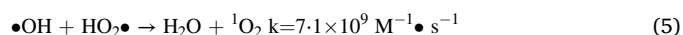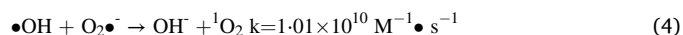
Fig. 4. (a) The performance of different catalysts for NO removal; (b) the influence of urea ratio on NO removal efficiency; (c) the influence of H_2O_2 concentration on NO removal efficiency and H_2O_2/NO molar ration; (d) influences of temperature; (e) flue gas components (NO, O_2, SO_2 and CO_2) on the NO removal efficiency; (f) the reusability of 2.5 U-LaFeO$_3$ catalyst for NO removal process. Reaction conditions: NO concentration, 350 ppm; catalyst mass, 0.1 g; balance gas, N_2; gas flow, GHSV= 77,000 h^{-1}, temperature, 120 °C.

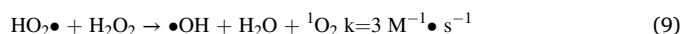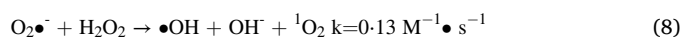### 3.3. ROS determination and generation mechanisms

EPR tests were firstly performed to determine the ROS types in 2.5 U-LaFeO$_3$/H$_2$O$_2$. The fingerprint peaks of DMPO-OH (1:2:2:1), DMPO-O$_2$•⁻ (sextet line signals) and 2,2,6,6-tetramethyl-4-piperidinol-*N*-oxyl (TEMPO, triple line signals) adducts appear in Fig. 5(a), confirming the formations of •OH, O$_2$•⁻ and ¹O$_2$ [47], and the peak intensities of ¹O$_2$ and O$_2$•⁻ are higher than those of •OH, suggesting that ¹O$_2$ and O$_2$•⁻ are the major ROS. In Fig. S14, the peaks intensity gradually enlarges as the reaction time increases from 1 min to 10 min, implying their longer presence and continual generation with the reaction time. To evaluate the contributions of •OH, O$_2$•⁻ and ¹O$_2$ to the NO removal, radical quenching tests were further carried out by using tert-butanol (TBA), p-benzoquinone (BQ) and furfuryl alcohol (FFA) as the scavengers, respectively [48]. In Fig. 5(b), adding TBA, BQ and FFA all reduce the NO removal efficiency, and the inhibitory rate in descending order is FFA (53.66%) > BQ (19.53%) > TBA (10.22%), indicating that the contribution order of ROS to NO removal is ¹O$_2$ > O$_2$•⁻ > •OH. To confirm whether TBA, BQ and FFA consume H$_2$O$_2$, the H$_2$O$_2$ content in H$_2$O$_2$, H$_2$O$_2$ + FFA and H$_2$O$_2$ + BQ systems was determined using the KMnO$_4$ titration method in Fig. S15 (Text S2), and the results showed that FFA or BQ did not consume H$_2$O$_2$ and only acted as the radical quencher. Besides, ozone (O$_3$) concentration in this system was detected (Fig. S16): the steady O$_3$ concentration was only 1.81 ppm, so its contribution to NO removal (350 ppm) was negligible. The EPR spectra of ¹O$_2$ under O$_2$ atmosphere is also provided in Fig. S17: only a weak peak signal appears at the beginning, and the existence time was too short to maintain NO removal. Given the facts that ¹O$_2$ dominated the NO removal process and H$_2$O$_2$ was the sole ROS precursor in this system (N$_2$ atmosphere), three possible reaction pathways of H$_2$O$_2$ deriving into ¹O$_2$ were summarized in Fig. S18: (i) the radical self-quenching reactions including the recombination of O$_2$•⁻ and HO$_2$•, and the reactions between O$_2$•⁻/HO$_2$• and •OH (Eqs. 4–7) [49,50]; (ii) the Haber-Weiss reaction between O$_2$•⁻/HO$_2$• and H$_2$O$_2$ (Eqs. 8–9) [51,52]; (iii) the oxidation reaction between high-valent metal cations and O$_2$•⁻ (Eqs.

10–11) [20,21].

Path i:

$$\bullet OH + O_2\bullet^- \rightarrow OH^- + {}^1O_2 \quad k=1\cdot01\times10^{10} \ M^{-1}\bullet s^{-1} \qquad (4)$$

$$\bullet OH + HO_2\bullet \rightarrow H_2O + {}^1O_2 \quad k=7\cdot1\times10^9 \ M^{-1}\bullet s^{-1} \qquad (5)$$

$$O_2\bullet^- + HO_2\bullet \rightarrow HO_2^- + {}^1O_2 \quad k=9\cdot7\times10^7 \ M^{-1}\bullet s^{-1} \qquad (6)$$

$$HO_2\bullet + HO_2\bullet \rightarrow H_2O_2 + {}^1O_2 \quad k=8\cdot3\times10^5 \ M^{-1}\bullet s^{-1} \qquad (7)$$

Path ii:

$$O_2\bullet^- + H_2O_2 \rightarrow \bullet OH + OH^- + {}^1O_2 \quad k=0\cdot13 \ M^{-1}\bullet s^{-1} \qquad (8)$$

$$HO_2\bullet + H_2O_2 \rightarrow \bullet OH + H_2O + {}^1O_2 \quad k=3 \ M^{-1}\bullet s^{-1} \qquad (9)$$

Path iii:

$$M^{4+}/M^{3+} + O_2\bullet^- \rightarrow M^{2+} + {}^1O_2 \qquad (10)$$
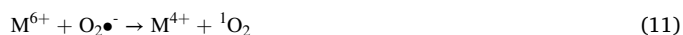
$$M^{6+} + O_2\bullet^- \rightarrow M^{4+} + {}^1O_2 \qquad (11)$$

In Paths (i) and (ii), the rate constants involving •OH (Eqs. 4–5) for ¹O$_2$ generation are far higher than others (Eqs. 6–9), so we firstly determined if •OH contributed the most to the ¹O$_2$ yield. In Fig. 5(c), when 90 mM TBA is added in the 2.5 U-LaFeO$_3$/H$_2$O$_2$, the EPR signal intensity of TEMPO is unchanged, indicating that the reactions between O$_2$•⁻/HO$_2$• and •OH are helpless for ¹O$_2$ generation. Besides, in Path (ii) the Haber-Weiss reaction is highly dependent on the high concentration of H$_2$O$_2$ [47,50], so we studied the contribution rate of ¹O$_2$ to the NO removal under different H$_2$O$_2$ concentrations. In Fig. 5(d), as the H$_2$O$_2$ concentration increases by 2 times, the ¹O$_2$ contribution rate to the NO removal decreases by 9.1% instead, indicating that the concentration of H$_2$O$_2$ was not the primary factor dominating the ¹O$_2$ yield.

Learned from the above analyses, Path (iii) is the most probability. To prove this, we added BQ to quench O$_2$•⁻ to suppress its reaction with Fe(III) and Fe(IV). In Fig. 5(c), after adding 90 mM BQ, the signal intensity of TEMPO dramatically decreases, confirming the involvement of
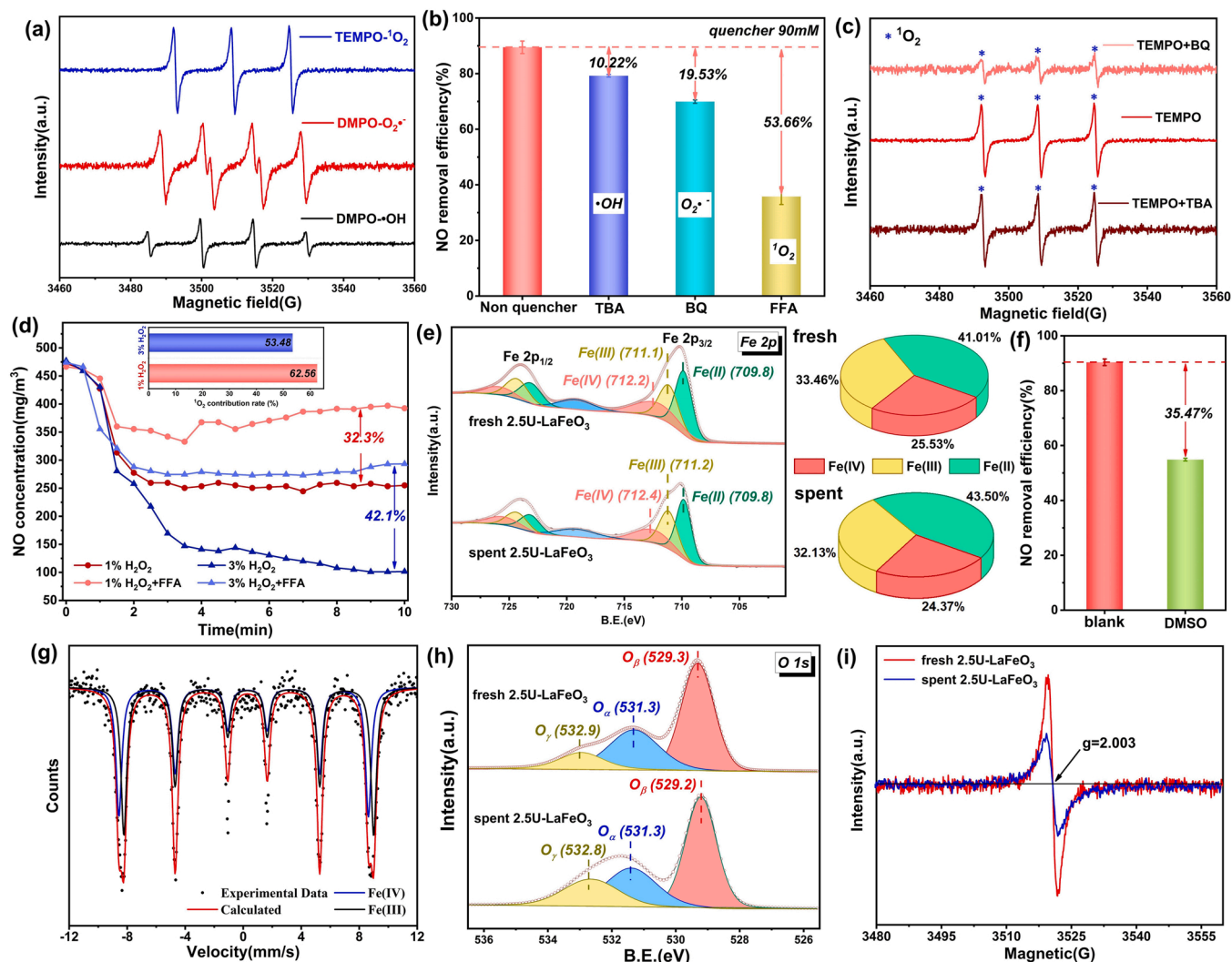
Fig. 5. (a) EPR spectra of the activated H_2O_2 system using DMPO and TEMP spin-trapping; (b) The radical scavenging experiments during NO removal; (c) EPR spectra of $^1O_2$ in the presence of BQ and TBA; (d) quenching experiments with FFA as the scavenger under 1% and 3% H_2O_2 concentrations; the XPS spectra of fresh and spent 2.5 U-LaFeO$_3$: (e) Fe 2p; and (h) O 1 s; (f) DMSO quenching experiment during NO removal; (g) Mössbauer spectrum of 2.5 U-LaFeO$_3$; (i) EPR profiles of fresh and spent 2.5 U-LaFeO$_3$.

$O_2\bullet^-$ in $^1O_2$ generation. Moreover, in Fig. 5(e) the Fe 2p XPS analyses of the fresh and spent 2.5 U-LaFeO$_3$ also illuminate that after reaction the proportions of Fe(IV) and Fe(III) decrease from 25.53% to 24.37% and from 33.46% to 32.13%, respectively, while that of Fe(II) increases from 41.01% to 43.50%. To solidly verify the involvement of Fe(IV)/Fe(III) in $^1O_2$ generation, the Mössbauer spectroscopy analysis and DMSO quenching experiment were further conducted. In Mössbauer spectroscopy, the isomer shifts (IS) can describe the charge density of the electron cloud around the charge and characterize the electrostatic interactions, so the valence state of material can be obtained according to IS [53]. DMSO, as a reductant, can reduce Fe(IV) to Fe(II) via a 2-electron transfer step [54,55], thereby reducing the content of Fe(IV) in material. In Fig. 5(g) and Table S4, it can be found from the Mössbauer spectrum of 2.5 U-LaFeO$_3$ that two isomer shifts appear, i.e. 0.34 and 0.16, representing the Fe(III) and Fe(IV) species, respectively [56,57]. In Fig. 5(f), after adding 0.36 M DMSO, the NO removal efficiency decreases by 35.47%, confirming the existence and the function of Fe(IV) in the heterogeneous Fenton denitrification reaction. Hence, the above analyses manifested that $O_2\bullet^-$+Fe(IV)/Fe(III) is the main generation path of $^1O_2$.

To reveal the roles of each component of 2.5 U-LaFeO$_3$ in heterogeneous Fenton reaction, the elemental valence evolution of La and O in the fresh and spent 2.5 U-LaFeO$_3$ catalysts were illuminated by XPS. In Fig. S19 and Table S2, the proportions of La(II) and La(III) are unchanged before and after the reaction, indicating that La was not involved in reaction [27,33]. But in Fig. 5(h) and Table S2, the proportion of O_α decreases from 34.16% to 28.49%, while that of O_β increases from 51.74% to 55.53%, indicating that the surface chemisorbed oxygen was consumed, whereas OV converted into the lattice oxygen by grabbing an O atom. To confirm this, we used EPR method to determine the OV's quantity in the fresh and spent 2.5 U-LaFeO$_3$. In Fig. 5(i), after reaction the OV's quantity decreases by a half (from 19852.46 to 9319.71), thus OV was definitely involved in the heterogeneous Fenton reaction and might serve as one of the adsorption sites for O-containing reactants [31].

3.4. Theoretical calculation and denitrification mechanisms

DFT calculations were used to study the heterogeneous Fenton mechanism, and the surface model of the (110) facet of LaFeO$_3$, La$_{0.9}$FeO$_3$ and 2.5 U-LaFeO$_3$ was built. Firstly, two thermodynamically stable adsorption configurations of H_2O_2 on three catalysts were constructed in Fig. 6(a) and (b). In configuration (a), H_2O_2 can be decomposed into two -OH on a Fe atom, and the adsorption energies (E_{ads}) are
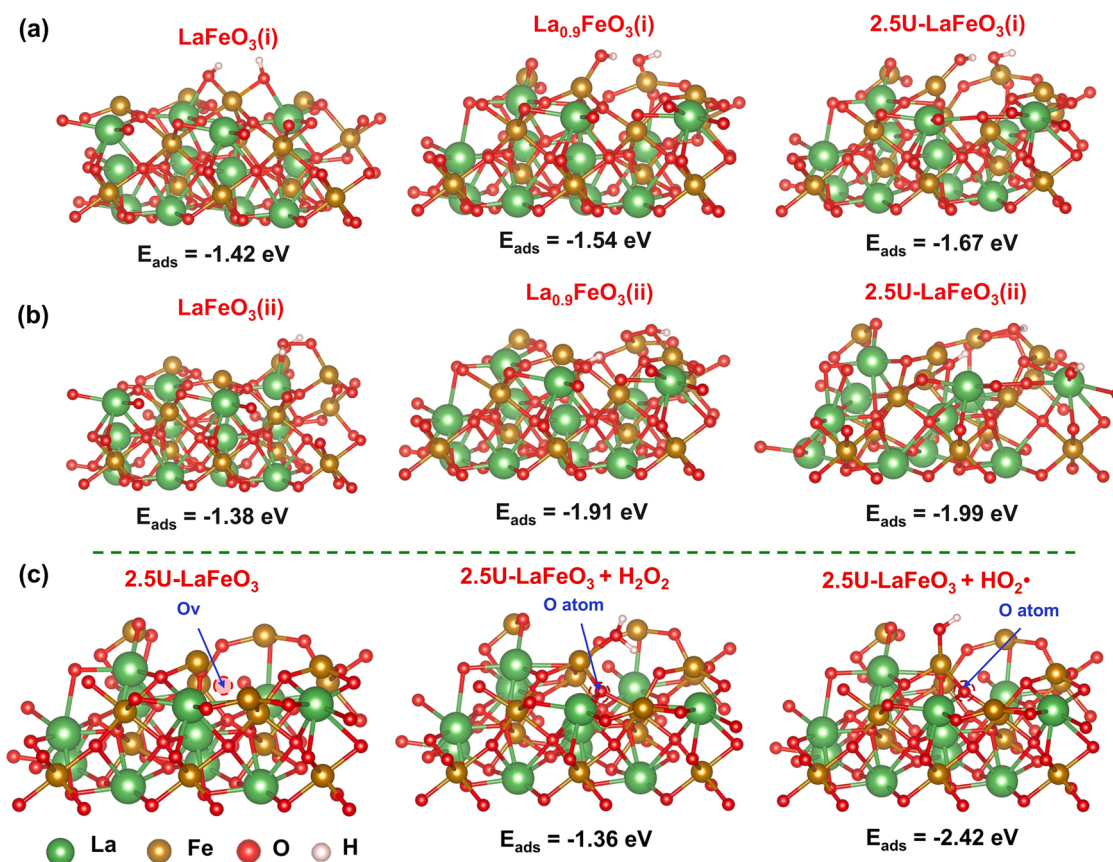
Fig. 6. (a, b) The configurations of H_2O_2 adsorption on $LaFeO_3$ (110), $La_{0.9}FeO_3$ (110) and 2.5 U-$LaFeO_3$ (110) surface; (c) the configurations of H_2O_2 and $HO_2\bullet$ adsorption on OV site of 2.5 U-$LaFeO_3$.

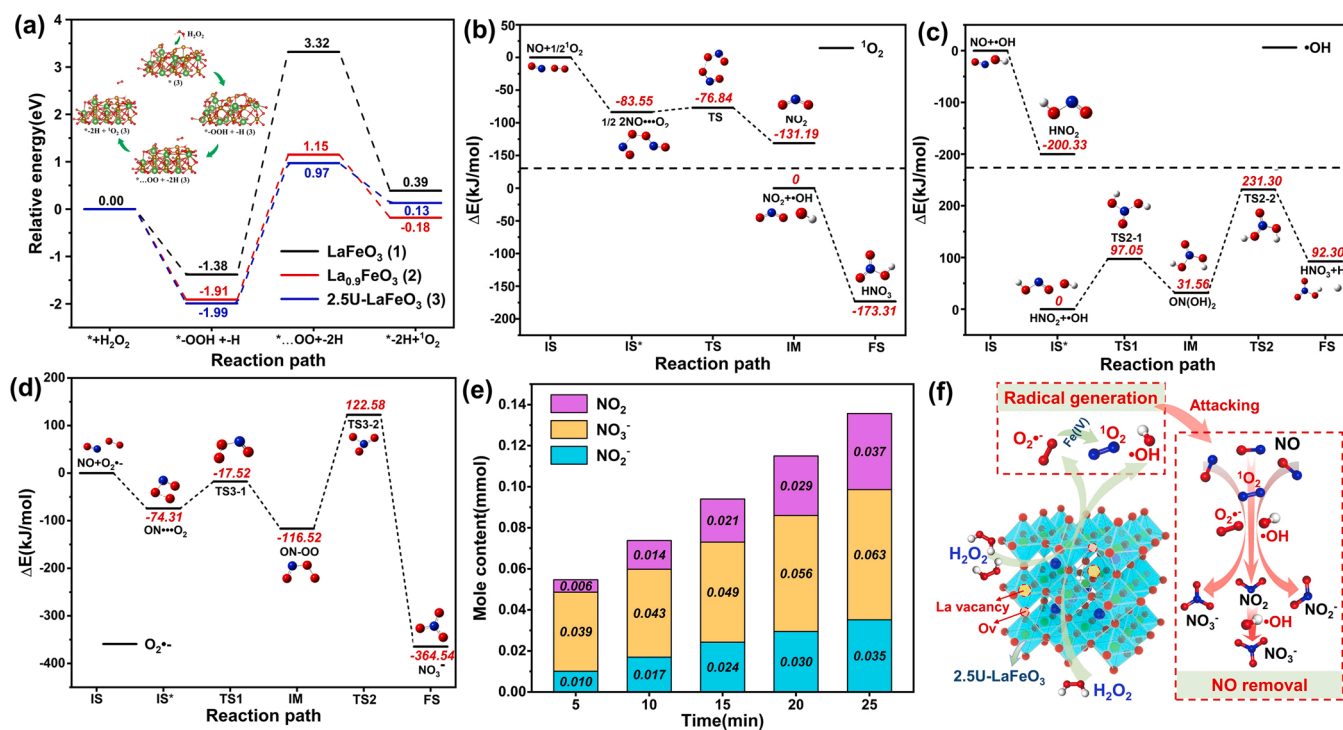**Fig. 7.** (a) The energy variation along reaction paths over $LaFeO_3$, $La_{0.9}FeO_3$ and 2.5 U-$LaFeO_3$ activating H_2O_2; theoretical calculation on (b) $^1O_2$, (c) $\bullet OH$ and (d) $O_2\bullet^-$ initiated NO removal reactions; (e) the distribution and variation of N species in the tail gas and absorption liquid; (f) mechanism schematic of NO removal by 2.5 U-$LaFeO_3$/H_2O_2.

− 1.42, − 1.54 and − 1.67 eV for $LaFeO_3$, $La_{0.9}FeO_3$ and 2.5 U-$LaFeO_3$, respectively. In configuration (b), H_2O_2 is decomposed into a HO_2- on a Fe atom and a -H on the bridge O atom of FeO_6 octahedron, the corresponding E_{ads} are − 1.38, − 1.91 and − 1.99 eV. The results indicated that the two reactions could proceed spontaneously, but the configuration (b) was more thermodynamically favorable. Moreover, the lowest E_{ads} of H_2O_2 on 2.5 U-$LaFeO_3$ suggested that urea-modulated $LaFeO_3$ was superior to $LaFeO_3$ and $La_{0.9}FeO_3$ in activating H_2O_2, which was mainly due to 2.5 U-$LaFeO_3$ had more OV sites, as proved by the DFT calculation and EPR analysis. To demonstrate the promotion of OV, the adsorption configurations of H_2O_2 and HO_2- on OV of 2.5 U-$LaFeO_3$ were constructed in Fig. 6(c). The results suggested that OV could trap an O atom from H_2O_2 or HO_2-, which then decomposed into H_2O and •OH (on Fe atom), respectively, and the corresponding E_{ads} are − 1.36 and − 2.42 eV, so OV was easily to adsorb HO_2- instead of H_2O_2. Therefore, the •OH generation path could be concluded as following two: (i) Fe site could directly split H_2O_2 into two •OH; (ii) OV site decomposed the intermediate HO_2- into •OH.

To depict the $^1O_2$ generation path, the transition state (TS) theory was used to calculate the energy variations along the reaction paths over $LaFeO_3$, $La_{0.9}FeO_3$ and 2.5 U-$LaFeO_3$, and the relevant energy and structural variations are presented in Fig. 7(a) and S20, respectively. With the configuration (b) in Fig. 6 as the adsorption model, H_2O_2 will be firstly adsorbed on the catalyst's slab (*) and decomposed into * -OOH and -H; afterwards the * -OOH will convert into the transition state * …OO; finally $^1O_2$ will be formed via electron transfer with Fe (IV)/Fe(III). Additionally, the order of the energy barrier from * -OOH to * …OO is 4.70 eV ($LaFeO_3$) > 3.06 eV ($La_{0.9}FeO_3$) > 2.96 eV (2.5 U-$LaFeO_3$), indicating that both urea modulation and non-stoichiometric synthesis methods could improve the catalytic activity but urea modulation was better. Hence, the urea modulation method can not only enhance the adsorption capacity toward H_2O_2, but also reduce the reaction energy barrier for $^1O_2$ generation.

Then the mechanism of NO removal induced by •OH, O_2•- and $^1O_2$ were depicted by using Gaussian 09 software. In Fig. 7(b), $^1O_2$ can react with two NO to form a complex ON•••O-O•••NO, and then the O-O bond will be broken after undergoing a TS with the ΔE of only 6.71 kJ/mol, finally two NO_2 are formed. Subsequently, the formed NO_2 can spontaneously react with •OH to produce a HNO_3. In Fig. 7(c), •OH can spontaneously react with NO to form a HNO_2, then the formed HNO_2 continually reacts with a •OH to produce a HNO_3, but the ΔE values for TS2–1 (from HO-ON•••OH to ON(OH)$_2$) and TS2–2 (from ON(OH)$_2$ to HNO_3) are as high as 97.05 kJ/mol and 199.74 kJ/mol, respectively. In Fig. 7(d), O_2•- can spontaneously react with NO to form a complex ON•••O_2, which then evolves into the intermediate ON-OO via TS3–1 ($\Delta E = 56.11$ kJ/mol). Finally, undergoing TS3–2 ($\Delta E = 239.10$ kJ/mol), the N-O bond in ON-OO is rotated, the O-O bond is elongated and the terminal O atom approaches N to form N-O, while the O-O bond breaks, NO_3 is formed eventually. In summary, $^1O_2$ was responsible to the formation of NO_2, while •OH and O_2•- mainly contributed to the formations of NO_2 and NO_3; the reactivity of the three ROS towards NO is $^1O_2$ > •OH > O_2•- according to the ΔE values; the main generation path for NO_3 could be NO_2 + •OH due to its lowest ΔE value; •OH played two major roles in the NO removal process: (i) direct oxidation of NO into NO_2; (ii) secondary oxidation of NO_2 into NO_3.

To identify the distribution and variation of N species in the system, the contents of NO_2, NO_2^- and NO_3^- in the tail gas and the absorption liquid were detected. In Fig. 7(e) and S21, as the reaction proceeds from 5 to 15 and 25 min, the proportion of NO_2 increases from 10.98% to 22.33% and 27.28%, while that of NO_3^- decreases from 70.53% to 51.87% and 46.79%, and that of NO_2^- slightly increases from 18.50% to 25.80% and 25.93%. The results implied that as the reaction proceeded, the quantity of •OH was insufficient to eliminate all NO_2, and •OH was inclined to directly react with NO to form NO_2 instead of with NO_2 to form NO_3^-, which was mainly due to their difference in ΔE values (−200.33 eV vs −173.31 eV). But it was worth noting that although the

proportion of NO_3^- decreased gradually with the reaction, it was still the main N-product. In Fig. S22, if the absorption liquid was added with Na_2SO_3, the main N product turned from NO_3^- to NO_2^-, and only a little NO_2 was emitted, which was resulted from the redox reaction between NO_2 and SO_3^{2-} [58]. The overall mechanisms of NO removal by 2.5 U-$LaFeO_3$/H_2O_2 are depicted in Fig. 7(f): (i) *Radical generation*: the 2.5 U-$LaFeO_3$ catalyst firstly adsorbs and decomposes H_2O_2 into •OH and HO_2•/O_2•-, then OV catalyzes HO_2• to generate HO•, and Fe(IV)/Fe (III) catalyze O_2•- to produce $^1O_2$. (ii) *NO removal*: the generated •OH, O_2•- and $^1O_2$ selectively oxidize NO into NO_2, NO_3^- and NO_2^-, in which the reactions of NO+$^1O_2$, NO_2 + •OH and NO+ •OH are the main pathways for the NO removal; O_2•- is mainly acted as the precursor of $^1O_2$ instead of an oxidant directly oxidizing NO into NO_3^-.

4. Conclusions

This study fabricates a urea-modulated perovskite catalyst 2.5 U-$LaFeO_3$, which can generate abundant $^1O_2$ in the heterogeneous Fenton system, different from the conventional •OH-dominated Fenton reaction. A series of characterization methods confirmed that 2.5 U-$LaFeO_3$ had abundant La defects, OVs and Fe(IV) active sites, and the urea modulation also improved the pore structure of perovskite and increased the specific surface area, thus enhancing the absorption, splitting and utilization of H_2O_2. The $LaFeO_3$/H_2O_2 system could achieve cost-effective removal of NO (82.9%) at high GHSV (30,800 h^{-1}) and low H_2O_2/NO molar ratio (4.7), along with good environmental adaptability and reusability. $^1O_2$, O_2•- and •OH were the main radicals generated in this reaction system, among which $^1O_2$ was superior to other radicals in NO removal. Combined the characterization and theoretical calculations, the $^1O_2$ generation route in the 2.5 U-$LaFeO_3$/H_2O_2 system and the NO removal mechanisms induced by $^1O_2$, O_2•- and •OH were systematically depicted. Urea-modulated $LaFeO_3$ perovskite material is a superior, cost-efficient and simple-synthesis catalyst, which can provide a feasible and promising strategy for the development of heterogeneous Fenton denitrification technology.

CRediT authorship contribution statement

Zhen Qian: Data curation, Validation, Formal analysis, Writing – original draft. **Mengchao Luo:** Data curation, Visualization. **Xiaohe Feng:** Data curation. **Xiaojie Yang:** Data curation. **Yongxue Guo:** Data curation. **Lijuan Yang:** Supervision, Conceptualization. **Bo Yuan:** Supervision, Investigation. **Yi Zhao:** Resources, Supervision. **Runlong Hao:** Project administration, Funding acquisition, Writing – review & editing.

Declaration of Competing Interest

The authors declare that they have no known competing financial interests or personal relationships that could have appeared to influence the work reported in this paper.

Data Availability

Data will be made available on request.

Acknowledgments

Appendix A. Supporting information

Supplementary data associated with this article can be found in the online version at doi:10.1016/j.apcatb.2023.123042.

References

[1] R. Hailili, H. Ji, K. Wang, X. Dong, C. Chen, H. Sheng, D.W. Bahnemann, J. Zhao, ZnO with controllable oxygen vacancies for photocatalytic nitrogen oxide removal, ACS Catal. 12 (2022) 10004–10017.

[2] S. Chen, Y. Zhou, J. Li, Z. Hu, F. Dong, Y. Hu, H. Wang, L. Wang, K.K. Ostrikov, Z. Wu, Single-atom Ru-implanted metal–organic framework/MnO$_2$ for the highly selective oxidation of NO$_x$ by plasma activation, ACS Catal. 10 (2020) 10185–10196.

[3] J. Zhao, Y. Xia, M. Li, S. Li, W. Li, S. Zhang, A biophysicochemical model for NO removal by the chemical absorption-biological reduction integrated process, Environ. Sci. Technol. 50 (2016) 8705–8712.

[4] C. Chen, Y. Cao, S. Liu, J. Chen, W. Jia, Review on the latest developments in modified vanadium-titanium-based SCR Catalysts, Chin. J. Catal. 39 (2018) 1347–1365.

[5] S. Zhang, Y. Zhao, J. Yang, J. Zhang, C. Zheng, Fe-modified MnO$_x$/TiO$_2$ as the SCR Catalyst for simultaneous removal of NO and mercury from coal combustion flue gas, Chem. Eng. J. 348 (2018) 618–629.

[6] S. Sun, J. Zhang, C. Sheng, H. Zhong, The removal of NO from flue gas by NaOH-catalyzed H$_2$O$_2$ system: mechanism exploration and primary experiment, J. Hazard. Mater. 440 (2022) 129788.

[7] B. Yuan, Z. Qian, Q. Yu, R. Hao, Y. Zhao, Ultraviolet-induced nitric oxide removal using H$_2$O/O$_2$ catalyzed by Fe/TiO$_2$: feasibility and prospect, Fuel 290 (2021), 120026.

[8] Y. Liu, J. Zhang, C. Sheng, Y. Zhang, L. Zhao, Simultaneous removal of NO and SO$_2$ from coal-fired flue gas by UV/H$_2$O$_2$ advanced oxidation process, Chem. Eng. J. 162 (2010) 1006–1011.

[9] R. Matta, K. Hanna, T. Kone, S. Chiron, Oxidation of 2,4,6-trinitrotoluene in the presence of different iron-bearing minerals at neutral pH, Chem. Eng. J. 144 (2008) 453–458.

[10] Y. Zhao, B. Yuan, R. Hao, Z. Tao, Low-temperature conversion of NO in flue gas by vaporized H$_2$O$_2$ and nanoscale zerovalent iron, Energy Fuels 31 (2017) 7282–7289.

[11] B. Wu, S. Zhang, S. He, Y. Xiong, Follow-up mechanism study on NO oxidation with vaporized H$_2$O$_2$ catalyzed by Fe$_2$O$_3$ in a fixed-bed reactor, Chem. Eng. J. 356 (2019) 662–672.

[12] X. Huang, J. Ding, Q. Zhong, Catalytic decomposition of H$_2$O$_2$ over Fe-based catalysts for simultaneous removal of NO$_x$ and SO$_2$, Appl. Surf. Sci. 326 (2015) 66–72.

[13] B. Yuan, X. Mao, Z. Wang, R. Hao, Y. Zhao, Radical-induced oxidation removal of multi-air-pollutant: a critical review, J. Hazard. Mater. 383 (2020), 121162.

[14] S.N. Batchelor, D. Carr, C.E. Coleman, L. Fairclough, A. Jarvis, The photofading mechanism of commercial reactive dyes on cotton, Dyes Pigments 59 (2003) 269–275.

[15] P. Hong, Z. Wu, D. Yang, K. Zhang, J. He, Y. Li, C. Xie, W. Yang, Y. Yang, L. Kong, J. Liu, Efficient generation of singlet oxygen (^{1}O$_2$) by hollow amorphous Co/C composites for selective degradation of oxytetracycline via Fenton-like process, Chem. Eng. J. 421 (2021), 129594.

[16] X. Mi, P. Wang, S. Xu, L. Su, H. Zhong, H. Wang, Y. Li, S. Zhang, Almost 100% peroxymonosulfate conversion to singlet oxygen on single-atom CoN$_{2+2}$ sites, Angew. Chem. Int. Ed. 60 (2021) 4588–4593.

[17] F. Chen, L. Liu, J. Chen, W. Li, Y. Chen, Y. Zhang, J. Wu, S. Mei, Q. Yang, H. Yu, Efficient decontamination of organic pollutants under high salinity conditions by a nonradical peroxymonosulfate activation system, Water Res. 191 (2021) 116799.

[18] P. Yang, W. Long, W. Huang, D. Liu, Single-atom copper embedded in two-dimensional MXene toward peroxymonosulfate activation to generate singlet oxygen with nearly 100% selectivity for enhanced Fenton-like reactions, Appl. Catal. B 324 (2023) 122245.

[19] B. Sheng, C. Deng, Y. Li, S. Xie, Z. Wang, H. Sheng, J. Zhao, In situ hydroxylation of a single-atom iron catalyst for preferential ^{1}O$_2$ production from H$_2$O$_2$, ACS Catal. 12 (2022) 14679–14688.

[20] J. Ji, Q. Yan, P. Yin, S. Mine, M. Matsuoka, M. Xing, Defects on CoS$_{2-x}$: tuning redox reactions for sustainable degradation of organic pollutants, Angew. Chem. Int. Ed. 60 (2021) 2903–2908.

[21] Q. Yi, J. Ji, B. Shen, C. Dong, J. Liu, J. Zhang, M. Xing, Singlet oxygen triggered by superoxide radicals in a molybdenum cocatalytic Fenton reaction with enhanced REDOX activity in the environment, Environ. Sci. Technol. 53 (2019) 9725–9733.

[22] R. Ji, J. Chen, T. Liu, X. Zhou, Y. Zhang, Critical review of perovskites-based advanced oxidation processes for wastewater treatment: operational parameters, reaction mechanisms, and prospects, Chin. Chem. Lett. 33 (2021) 643–652.

[23] Y. Zheng, R. Zhang, L. Zhang, Q. Gu, Z. Qiao, A resol-assisted cationic coordinative co-assembly approach to mesoporous ABO$_3$ perovskite oxides with rich oxygen vacancy for enhanced hydrogenation of furfural to furfuryl alcohol, Angew. Chem. Int. Ed. 60 (2021) 4774–4781.

[24] A. Kumar, A. Kumar, V. Krishnan, Perovskite oxide based materials for energy and environment-oriented photocatalysis, ACS Catal. 10 (2020) 10253–10315.

[25] C. Cheng, S. Gao, J. Zhu, G. Wang, L. Wang, X. Xia, Enhanced performance of LaFeO$_3$ perovskite for peroxymonosulfate activation through strontium doping towards 2,4-D degradation, Chem. Eng. J. 384 (2020), 123377.

[26] K. Pan, K. Hou, J. Hu, J. Yang, J. Xiang, C. Li, C. Xu, S. Chen, S. Liang, J. Yang, Ca and Cu doped LaFeO$_3$ to promote coupling of photon carriers and redox cycling for facile photo-Fenton degradation of bisphenol A, Chemosphere 308 (2022), 136325.

[27] J. Li, J. Miao, X. Duan, J. Dai, Q. Liu, S. Wang, W. Zhou, Z. Shao, Fine-tuning surface properties of perovskites via nanocompositing with inert oxide toward developing superior catalysts for advanced oxidation, Adv. Funct. Mater. 28 (2018) 1804654.

[28] X. Li, M. Li, X. Ma, J. Miao, R. Ran, W. Zhou, S. Wang, Z. Shao, Nonstoichiometric perovskite for enhanced catalytic oxidation through excess A-site cation, Chem. Eng. Sci. 219 (2020), 115596.

[29] X. Liu, J. Mi, L. Shi, H. Liu, J. Liu, Y. Ding, J. Shi, M. He, Z. Wang, S. Xiong, Q. Zhang, Y. Liu, Z. Wu, J. Chen, J. Li, In situ modulation of A-site vacancies in LaMnO$_{3.15}$ perovskite for surface lattice oxygen activation and boosted redox reactions, Angew. Chem. Int. Ed. 60 (2021) 26747–26754.

[30] W. Si, Y. Wang, Y. Peng, J. Li, Selective dissolution of A-site cations in ABO$_3$ perovskites: a new path to high-performance catalysts, Angew. Chem. Int. Ed. 127 (2015) 7954–7957.

[31] C. Feng, Q. Gao, G. Xiong, Y. Chen, Y. Pan, Z. Fei, Y. Li, Y. Lu, C. Liu, Y. Liu, Defect engineering technique for the fabrication of LaCoO$_3$ perovskite catalyst via urea treatment for total oxidation of propane, Appl. Catal., B 304 (2022), 121005.

[32] N. Guo, L. Jiang, D. Wang, Y. Zhan, Z. Wang, Selective modulation of La-site vacancies in La$_{0.9}$Ca$_{0.1}$MnO$_3$ perovskites catalysts for toluene oxidation: the role of oxygen species on the catalytic mechanism, Sep. Purif. Technol. 310 (2023), 123227.

[33] Y. Nie, L. Zhang, Y. Li, C. Hu, Enhanced Fenton-Like degradation of refractory organic compounds by surface complex formation of LaFeO$_3$ and H$_2$O$_2$, J. Hazard. Mater. 294 (2015) 195–200.

[34] C. Liu, K. Xiang, J. Li, H. Liu, F. Shen, Controllable disordered copper sulfide with a sulfur-rich interface for high-performance gaseous elemental mercury capture, Environ. Sci. Technol. 56 (2022) 13664–13674.

[35] J. Cai, Y. Xia, R. Gang, S. He, S. Komarneni, Activation of MoS$_2$ via tungsten doping for efficient photocatalytic oxidation of gaseous mercury, Appl. Catal., B 314 (2022), 121486.

[36] R.L. Hao, Z. Qian, X. Yang, M. Luo, X. Feng, W. Qiao, Y. Zhao, B. Yuan, Enhanced removal of elemental mercury using MnO$_2$-modified molecular sieve under microwave irradiation, Chem. Eng. J. 450 (2022), 137997.

[37] Y. Yi, H. Liu, B. Chu, Z. Qin, L. Dong, H. He, C. Tang, M. Fan, L. Bin, Catalytic removal NO by CO over LaNi$_{0.5}$M$_{0.5}$O$_3$ (M = Co, Mn, Cu) perovskite oxide catalysts: tune surface chemical composition to improve N$_2$ selectivity, Chem. Eng. J. 369 (2019) 511–521.

[38] R. Sun, L. Shen, S. Wang, H. Bai, CO conversion over LaFeO$_3$ perovskite during chemical looping processes: influences of Ca-doping and oxygen species, Appl. Catal., B 316 (2022), 121598.

[39] M. Wu, S. Ma, S. Chen, W. Xiang, Fe–O terminated LaFeO$_3$ perovskite oxide surface for low temperature toluene oxidation, J. Clean. Prod. 277 (2020), 123224.

[40] S. Gong, Z. Xie, W. Li, X. Wu, N. Han, Y. Chen, Highly active and humidity resistive perovskite LaFeO$_3$ based catalysts for efficient ozone decomposition, Appl. Catal., B 241 (2019) 578–587.

[41] W. Yang, R. Zhang, B. Chen, D. Duprez, S. Royer, New aspects on the mechanism of C$_3$H$_6$ selective catalytic reduction of NO in the presence of O$_2$ over LaFe$_{1-x}$(Cu, Pd)$_x$O$_{3-\delta}$ perovskites, Environ. Sci. Technol. 46 (2012) 11280–11288.

[42] F. Fang, N. Feng, L. Wang, J. Meng, G. Liu, P. Zhao, P. Gao, J. Ding, H. Wan, G. Guan, Fabrication of perovskite-type macro/mesoporous La$_{1-x}$K$_x$FeO$_{3-\delta}$ nanotubes as an efficient catalyst for soot combustion, Appl. Catal., B 236 (2018) 184–194.

[43] M. Wu, S. Chen, W. Xiang, Oxygen vacancy induced performance enhancement of toluene catalytic oxidation using LaFeO$_3$ perovskite oxides, Chem. Eng. J. 387 (2020), 124101.

[44] K. Ji, H. Dai, J. Deng, L. Song, S. Xie, W. Han, Glucose-assisted hydrothermal preparation and catalytic performance of porous LaFeO$_3$ for toluene combustion, J. Solid State Chem. 199 (2013) 164–170.

[45] P. Yuan, Z. Wang, M.S. Ahmad, W. Kong, J. Ma, Z. Wang, B. Shen, Z. Ji, Enhanced oxidative removal of NO by UV/in situ Fenton: Factors, kinetics and simulation, Sci. Total. Environ. 778 (2021), 146202.

[46] R. Hao, Z. Wang, Y. Gong, Z. Ma, Z. Qian, Y. Luo, B. Yuan, Y. Zhao, Photocatalytic removal of NO and Hg0 using microwave induced ultraviolet irradiating H$_2$O/O$_2$ mixture, J. Hazard. Mater. 383 (2020), 121135.

[47] N. Zheng, X. He, R. Hu, R. Wang, Q. Zhou, Y. Lian, Z. Hu, In-situ production of singlet oxygen by dioxygen activation on iron phosphide for advanced oxidation processes, Appl. Catal., B 307 (2022), 121157.

[48] Y. Nosaka, A.Y. Nosaka, Generation and detection of reactive oxygen species in photocatalysis, Chem. Rev. 117 (2017) 11302–11336.

[49] J.D. Laat, H. Gallard, Catalytic decomposition of hydrogen peroxide by Fe(III) in homogeneous aqueous solution mechanism and kinetic modeling, Environ. Sci. Technol. 33 (1999) 2726–2732.

[50] R. Chen, J. Pignatello, Role of quinone intermediates as electron shuttles in Fenton and photoassisted Fenton oxidations of aromatic compounds, Environ. Sci. Technol. 31 (1997) 2399–2406.

[51] B. Bielski, D. Cabelli, R. Arudi, Reactivity of HO$_2$/O$_2$ radicals in aqueous solution, J. Phys. Chem. Ref. 14 (1985) 1041–1100.

[52] J.J. Pignatello, E. Oliveros, A. MacKay, Advanced oxidation processes for organic contaminant destruction based on the Fenton reaction and related chemistry, Crit. Rev. Environ. Sci. Technol. 36 (2006) 1–84.

[53] S. Liang, L. Zhu, J. Hua, W. Duan, P. Yang, S. Wang, C. Wei, C. Liu, C. Feng, Fe^{2+}/HClO reaction produces Fe^{IV}O^{2+}: an enhanced advanced oxidation process, Environ. Sci. Technol. 54 (2020) 6406–6414.

[54] Z. Yang, J. Qian, A. Yu, B. Pan, Singlet oxygen mediated iron-based Fenton-like catalysis under nanoconfinement, P. Natl. Acad. Sci. USA 116 (2019) 6659–6664.

[55] S. Pang, J. Jiang, J. Ma, Oxidation of sulfoxides and arsenic(III) in corrosion of nanoscale zero valent iron by oxygen: evidence against ferryl ions (Fe(IV)) as active intermediates in Fenton reaction, Environ. Sci. Technol. 45 (2011) 307–312.

[56] J. Chen, L. Dang, H. Liang, W. Bi, J.B. Gerken, S. Jin, E.E. Alp, S.S. Stahl, Operando analysis of NiFe and Fe oxyhydroxide electrocatalysts for water oxidation: detection of Fe^{4+} by mossbauer spectroscopy, J. Am. Chem. Soc. 137 (2015) 15090–15093.

[57] J. Wu, J.P. Dacquin, N. Djelal, C. Cordier, C. Dujardin, P. Granger, Calcium and copper substitution in stoichiometric and La-deficient LaFeO$_3$ compositions: a starting point in next generation of three-way-catalysts for gasoline engines, Appl. Catal., B 282 (2021), 119621.

[58] R. Hao, S. Yang, Y. Zhao, Y. Zhang, B. Yuan, X.Z. Mao, Follow-up research of ultraviolet catalyzing vaporized H$_2$O$_2$ for simultaneous removal of SO$_2$ and NO: absorption of NO$_2$ and NO by Na-based WFGD byproduct (Na$_2$SO$_3$), Fuel Process. Technol. 160 (2017) 64–69.